Geometric Active Learning for Segmentation of Large 3D Volumes

Thomas Lang, Tomas Sauer

Abstract—Segmentation, i.e., the partitioning of volumetric data into components, is a crucial task in many image processing applications ever since such data could be generated. Most existing applications nowadays, specifically CNNs, make use of voxelwise classification systems which need to be trained on a large number of annotated training volumes. However, in many practical applications such data sets are seldom available and the generation of annotations is time-consuming and cumbersome. In this paper, we introduce a novel voxelwise segmentation method based on active learning on geometric features. Our method uses interactively provided seed points to train a voxelwise classifier based entirely on local information. The combination of an ad hoc incorporation of domain knowledge and local processing results in a flexible yet efficient segmentation method that is applicable to three-dimensional volumes without size restrictions. We illustrate the potential and flexibility of our approach by applying it to selected computed tomography scans where we perform different segmentation tasks to scans from different domains and of different sizes.

Index Terms—Active Learning, Image Segmentation, Geometry, Interactive Algorithm, Support Vector Machines

◆

1 INTRODUCTION

E VER since the invention of computed tomography (CT) and the resulting generation of three-dimensional data, the extraction of certain components of such an image has been the core problem in different applications, among (many) others the detection of malign structures or visual inspection of selected parts. In clinical tomography, segmentation is a common task for which often large datasets, including annotated ground truth data, exist. In contrast, industrial applications typically not only generate much larger volumes at higher resolutions, at the same time annotated data is rarely available. Moreover, even the "certain" is uncertain in the sense that specifying what exactly has to be segmented from a volume is difficult in many applications. In other words, finding the right mode of user interaction also becomes an issue when dealing with industrial CT data.

This inhibits the usage of many modern segmentation methods including atlas-based methods or neural networks and their variants, since they, typically, require a large number of training samples including ground truth in order to learn properly. Another class of methods, including graph-based models and active contour methods, are of a *global* nature and thus are not appropriate for segmenting big volumes whose size can easily exceed the avaiable main memory. As a result, many applications are forced to rely on two-dimensional slice-wise image processing only, which easily overlooks thin three-dimensional structures. In addition, slice-based methods typically depend on the orientation of the object in the volume or of the object during the scan. Therefore, three-dimensional methods are preferable which in turn enforces us to perform local processing in order to handle large 3D volumes.

This paper introduces an active learning approach for interactive segmentation of three-dimensional volumes without size restrictions, hence constitutes an effort to overcome some limitations of related approaches. To minimize the user interaction and the amount of data needed for training, we decided to use a Support Vector Machine (SVM) with features that are designed to capture local structures. It is organized as follows. In Section 3, we first revisit feature design with an explicit emphasis on geometry. Next, we briefly recapitulate Support Vector Machines, after which we introduce our segmentation procedure. We will further give a coarse analysis of the algorithm's asymptotic runtime and memory behavior to show that our method is well suited for the segmentation of large volumes. In addition, we will also introduce a multiresolution segmentation scheme based on an iteration of our segmentation technique, which combines the advantage of faster volume processing with the flexibility of our SVM segmentation algorithm. We will intuitively describe that the multiscale procedure is also applicable to volumes without size restrictions. Section 4 shows the performance our scheme on selected datasets of different domains and sizes, illustrating both the segmentation performance as well as qualitative results. We will conclude our contributions in Section 5.

2 RELATED WORK

Active learning (AL) is an emerging branch of machine learning and particularly well suited for the segmentation of unknown objects where one lacks annotated training data. Existing work in the field of deep learning includes the 3D U-Net architecture [1] which features a neural network to be trained from few annotated slices while still obtaining

- *T. Lang is with FORWISS, University of Passau, and the Fraunhofer Institute of Integrated Circuits, Division Development Center X-ray Technology.*
  E-mail: langthom@forwiss.uni-passau.de
- *T. Sauer is with the Chair of Digital Image Processing & FORWISS, University of Passau, and the Fraunhofer Institute of Integrated Circuits, Division Development Center X-ray Technology.*
  E-mail: tomas.sauer@uni-passau.de

a dense three-dimensional segmentation result. More focussed on two-dimensional images than on volumes, the work of [2] uses a convolutional neural network approach that includes a probability map prediction from which a pixelwise uncertainty map is computed that serves as main indicator which yet unlabeled images should be interactively labeled next. In a similar way, [3] proposed a viewpoint learning approach in 2D images where view entropy and view divergence serve as indicators which superpixel shall be selected for labeling. From a medical perspective, [4] focusses on lung nodule detection and trains a conditional Generative Adversarial Network where the generator creates realistic X-ray images from which a Bayesian neural network computes its information content. The best images with respect to that metric are then added to the training dataset. Besides the popular neural network approaches, [5] proposed an active learning procedure for text processing, in which an optimal Support Vector Machine configuration is determined by actively labeling instances closest to the separating hyperplane. This method roughly corresponds to the popular uncertainty sampling which is widely used in active learning [6]. Similar approaches are used by [7] and [8], while [9] uses the same idea by selecting, in each iteration, a fixed size pool of unlabeled instances whose uncertainty is highest. While [7] describes a general way of how to employ active learning in combination with Support Vector Machines, [8] applies this to the field of image retrieval by using active learning to bootstrap the classifier. In contrast to that, [9] requires interactively labeled samples in order to adapt a classifier to a new domain. Another similar approach was proposed in [10] where an interactive SVM approach is used to delineate object boundaries. Returning to the field of image processing, [11] aims to segment an image pixelwise into multiple classes based on superpixel features. There, interactive user input in form of brush strokes serves as seed selection from which color features are extracted. A classifier is trained on these features and the given superpixels are classified with it. Switching to the three-dimensional case, [12] uses interactively provided markers as input for constructing a graph cut segmentation problem which upon solving partitions the dataset into the different categories of tumor, liver and other objects. One of the approaches closest to our method is [13] which incorporates geometric uncertainties into an active learning procedure in order to classify supervoxels. However, their work does not actually consider similarities to geometric primitives but rather constructs some uncertainty measure based on random walks to select the next supervoxels that shall be labeled.

The related approaches we mention above are still not applicable to our use case. The reason is that some of them require a full corpus of annotated training datasets, specifically the methods incorporating neural networks or atlas-based methods. In our situation, on the other hand, we often do not have any training data at all as many of the scans are unique. Approaches which aim for optimal segmentation by, e.g., using graph cut methods are not feasible as well for processing large volumes which may no longer fit into main memory. In this situation, constructing an even larger graph from the volume and searching for a globally optimal solution is unlikely to be processable. Instead, we focus on purely local processing and requesting as few labeling effort as possible. To do so, we increase the discriminative power of our classifier by explicitly using similarity of local regions to geometric primitives, which to our knowledge was not used elsewhere for segmentation purposes.

3 METHOD

Now we introduce our approach which combines both machine learning techniques and classical methods and is based on an active learning technique that incorporates explicit features by considering local geometry.

3.1 Geometric Features

Our classification system relies on features obtained from *local environments*. Precisely, around each voxel in the source volume, a small voxel environment of configurable size $K \times K \times K$, for $K > 1$ and odd, is used for the computation of features. The choice of K is a trade-off between locality and detectability of certain features and it needs to be chosen dependent on the *resolution*, not the *size* of the scan. As a rule of thumb, K should be large enough to distinguish between the basic features, like planarity, on a local basis, i.e., K should be larger than the thickness of what is considered to be an essentially two-dimensional object. If no full environment can be extracted, the voxel is not processed and the grayscale value at the according position in the target volume is set to zero. This is in accordance with our internal framework constraints but any other extension like padding can be incorporated as well with the usual price of boundary artifacts. In the sequel, we will briefly explain all features that we use, but we want to emphasize that not all features might be used for every scan. In practice, it turned out that a domain expert's proper choice of a subset of features best-suited to describe the selected regions can significantly accelerate the segmentation procedure. Alternatively, an automatic selection of relevant features is possible by linear standard methods like the PCA, see [14].

Roughly, we distinguish between structural and geometric features in our approach. *Structural features* capture properties of the grayscale distribution of the local environment by its first four standardized statistical moments [15]. Without a doubt, these are the features used most for grayscale image segmentation as they express the mean voxel value, the standard deviation of these values as well as the skewness and the (excess) kurtosis of the distribution of voxel values in the local region.

Depending on the concrete segmentation task, we may include the position of the current voxel as a somewhat trivial feature. But this can turn out to be useful if we try to separate objects touching each other or segment objects heavily distorted by artifacts, for example.

In addition, we aim to encode the structure of the local region using the well-known uniform local binary pattern for three orthogonal planes (LBP/TOP) [16], [17]. In this feature, one typically iterates over all pixels in a 2D region and computes the signature (either one or zero) of the difference of the current pixel value against the center of the region. The resulting bit string is converted into a single

integer. The uniform LBP version improves upon this by including that in piecewise homogenous regions which are common in industrial applications these bit strings are often of certain shapes only. The improvement considers only the changes between patterns which achieves some form of rotation invariance, cf. [18]. Since the LBP is classically defined for two-dimensional images only, we slightly altered the definition. First, we compute three projection images which are the sums along one axis at a time. For each projection image, an LBP descriptor is computed for each pixel in that image except at the boundary. These descriptors are aggregated in a histogram. The concatenation of the resulting three histograms form our structural feature.

Our main emphasis, however, lies on explicitly considering local geometry in order to provide a flexible way of learning shape properties. In particular, we include curvature as introduced in [19, Part IV.A] by iterating over each voxel inside the local environment and computing the curvature inside a smaller environment of dimensions $k \times k \times k$ around it, where the choice $k = 3$ performed well in our tests. The approach from [19] yields a voxel-based curvature estimation based on the second fundamental form without having to provide a threshold for the extraction of the surface. These curvature estimations are then aggregated in a histogram, thus effectively tracking the distribution of curvatures.

As a contrast to curvature, we also consider planar or linear structures which are particularly prominent in industrial applications. There, we consider the M nonzero voxels, more precisely, voxels above a certain threshold, inside the local environment and fit either a line or a plane to it by least squares regression. Having computed these structures, we collect the orthogonal distances of the nonzero voxels to the plane or line structures into a histogram of distances. Additionally, characteristics to represent planarity and width or linearity and diameter, respectively, are computed in the following way. We arrange the coordinates of these voxels columnwise in a matrix $C \in \mathbb{N}_0^{3 \times M}$, from which we compute the centered matrix $C' = C - M^{-1}C\mathbf{1}\mathbf{1}^T$, where $\mathbf{1}$ is the vector of ones. The three singular values of the matrix C' yield a simple but efficient orientation feature. With a singular value decomposition $C' = U\Sigma V^T$, we specifically need the column vector u_1 which points into the direction of the least squares fitting line, and u_3 which is the normal of the least squares fitting plane. For both structures we then use the current voxel as a point lying on it. Denote by L and P be these structures for linearity and planarity, respectively, and by D_L, D_P again the collections of orthogonal distances of the nonzero voxels to the structures [20] which we arrange in histograms $\mathcal{H}_L$ and $\mathcal{H}_P$, respectively. Moreover, we compute the characteristics

$$f_1^p = \exp\left(-\mathbb{E}[D_p]\right)$$
$$f_2^p = (2\sqrt{3}\lfloor K/2 \rfloor)^{-1}\left(\max_{d \in D_p} d - \min_{d \in D_p} d + 1\right)$$

for $p \in \{L, P\}$, where again K denotes the size of the local environment. The characteristic f_1^p tends to one for local linear or planar structures, $p = L$ or $p = P$, and to zero otherwise, hence it gives a measure for the linearity/planarity of the voxel region. The width of the

structure is indicated by f_2^p, whose denominator represents the maximum possible distance of a nonzero voxel in the local environment to a structure passing through the environment's center point. Eventually, the concatenation $(f_1^p, f_2^p, \mathcal{H}_p), p \in \{L, P\}$ forms our *linearity* and *planarity* features, respectively.

An alternative representation of planarity, linearity and also isotropy, is expressed via a variant of the inertia tensor as introduced in [21, Eq. 8.11]. This representation computes the Fourier tensor features from [22] efficiently in the spatial domain. A 3×3 inertia tensor is built from the partial derivatives giving a real symmetric matrix with three nonnegative eigenvalues $\lambda_1 \geq \lambda_2 \geq \lambda_3 \geq 0$, from which the geometric properties are computed as

$$f_l = \frac{\lambda_1 - \lambda_2}{\lambda_1}, \quad f_p = \frac{\lambda_2 - \lambda_3}{\lambda_1}, \quad f_s = \frac{\lambda_3}{\lambda_1}.$$

The ability to detect geometry from this feature is illustrated in Figure 1, where each voxel in a synthetic dataset is assigned the according feature value at the respective position. The *linearity* f_l is large if $\lambda_1 > \lambda_2 \approx \lambda_3 \approx 0$, i.e., when one direction of inertia is very prominent while the other dimensions are close to zero. A second dimension becomes prominent in the presence of planar structures, and we have $\lambda_1 \approx \lambda_2 > \lambda_3$ so that f_p approaches 1. Finally, homogenous structures are identified by the lack of a dominant direction, i.e., if all eigenvalues are approximately equal, in which case the *isotropy* f_s increases. Also note that the three nonnegative features add up to one and thus are normalized relative to each other in a natural way.

Yet another type of histogram feature we use, is a simple histogram of distances of nonzero voxels to the the center of the local environment as an indication of the overall geometry. We chose this as an alternative to the classical histogram of pairwise distances since the latter has a quadratic runtime with respect to the local environment size while the used feature is linear in it and thus easier to compute, in particular as the size of the local environment is K^3 already.

To incorporate orientation we rely on the classical Histogram of Oriented Gradients (HOG) as a feature. In its three-dimensional form, one considers the estimated gradient vector and its azimuthal and elevation angles which form a two-dimensional histogram where the according bin is incremented by the Euclidean norm of any gradient pointing in that direction. All orientations actually form a 3D sphere, but an equidistantly partitioned planar two-dimensional histogram would have bins at the "polar" regions where only very little orientations are covered. To compensate for this, we create a sphere histogram in which all cells have the same surface area. In the concrete application, we partitioned the elevation angles into five parts. The north-most and south-most sectors are further divided into four partitions while the three middle sectors are divided into 14 bins. Next, for each voxel in the local environment, we estimate the gradient at that point and compute the orientation angles from it. The bin identified by these angles is then incremented by the gradient magnitude provided that the latter is larger than some small threshold to reduce the influence of noise. The linearized sphere histogram then forms our HOG descriptor.
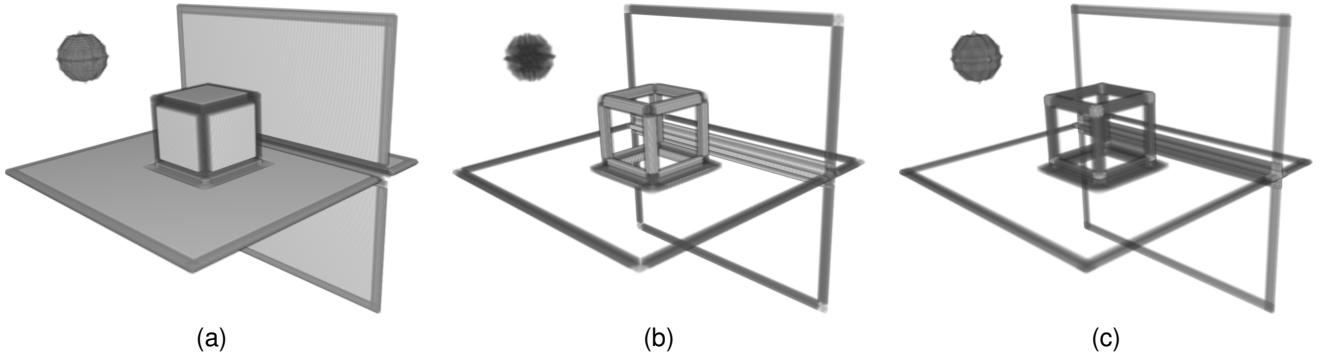
Fig. 1. Inertia tensor features detecting geometry on a synthetic dataset; brighter colors indicate higher values. (a) shows the planarity f_p which is high on the plane and also on the sides of the cube, (b) depicts the linearity f_l which enhances edges and (c) using f_s detects isotropic regions.

Regarding the usage of features, we want to point out two small but important caveats one has to take care of.

Firstly, scaling the features is very important when using a feature vector in a distance-based classifier, since one feature with a large variance can render other features useless although they are important geometry detectors. We recommend standardization of the features using the well-established z-score [23] technique on all features that belong together conceptually. Specifically, feature vector elements which stem from a histogram should be scaled using the same mean and standard deviation, while single values like the mean grayscale value, should just be scaled using the according parameters for this value.

Another more serious point is the comparison of histograms. It is well-known that histograms can and should be interpreted as discretized probability distributions and thus should ideally be compared using a metric suitable for distributions, e.g., the Wasserstein distance. We wish to make use of this metric, but distance-based classifiers typically consider Euclidean distances or inner products in Hilbert spaces only. To overcome this problem, we designed an embedding that transforms a histogram into a vector such that the Euclidean distance between two such vectors approximates the 2-Wasserstein distance between their original distributions.

Definition 1. For a probability measure μ on $\mathbb{R}$, we define the *Wasserstein embedding* of dimension $M \in \mathbb{N}$ as

$$\mathcal{E}_M(\mu) = \left(\langle F_\mu^{-1}, \xi_n \rangle \right)_{n=1}^M,$$

where $\{\xi_n\}_{n \in \mathbb{N}}$ is the classical Fourier basis of $L^2(0,1)$.

$\mathcal{E}_M$ basically computes the first M Fourier coefficients of the generalized inverse distribution function, also known as the *quantile function*, F_μ^{-1}, cf. [24]. With this embedding, we can use the 2-Wasserstein distance via a Euclidean distance.

Lemma 1. Let μ, ν be probability measures on $\mathbb{R}$ with associated quantile functions F_μ^{-1} and F_ν^{-1}, respectively. Assume that $g := F_\mu^{-1} - F_\nu^{-1} \in L^2(0,1)$, and denote by $W_2(\mu, \nu)$ the 2-Wasserstein distance between the probability measures. Then

$$\|\mathcal{E}_M(\mu) - \mathcal{E}_M(\nu)\|_2 \to W_2(\mu, \nu)$$

as $M \to \infty$.

Proof: In [25] it was shown that

$$W_2^2(\mu, \nu) = \int_0^1 \left| F_\mu^{-1}(x) - F_\nu^{-1}(x) \right|^2 \, dx.$$

Due to linearity of the inner product we have that

$$\|\mathcal{E}_M(\mu) - \mathcal{E}_M(\nu)\|_2^2 = \sum_{n=1}^M |\langle g, \xi_n \rangle|^2,$$

and for $M \to \infty$ we obtain pointwise convergence since

$$\lim_{M \to \infty} \sum_{n=1}^M |\langle g, \xi_n \rangle|^2 = \sum_{n=1}^\infty |\langle g, \xi_n \rangle|^2 = \|g\|_2^2 = W_2^2(\mu, \nu)$$

where we used Parseval's identity. □

While we specifically chose the classical Fourier basis of $L^2(0,1)$ by design, we remark that the pointwise convergence result holds for any orthonormal basis of this space. However, the choice of the well-known sine/cosine basis has the advantage that estimates can be made about the rate of convergence provided the function g satisfies some regularity conditions. For example, if both generalized inverse distribution functions are bounded, the Euclidean distance between embeddings converges linearly to the Wasserstein distance between the original measures. Moreover, as Fourier approximations are particularly well-suited for smooth functions even better rates of convergence can be obtained for embeddings over families of measures with smooth quantile functions.

3.2 Support Vector Machines

With a set of features with geometric relevance at hand, we decided to employ a Support Vector Machine classifier for the voxelwise decision making. SVMs are maximum margin classifiers which aim to separate two datasets in some feature space in the best possible way by a hyperplane while simultaneously allowing for some misclassifications during training in order to increase the robustness of the model, cf. [26]. In our work, we specifically used a variant called ν-SVM [27]. Denote by $\{(\boldsymbol{x}_i, y_i)\}_{i=1}^M$ a training dataset of samples $\boldsymbol{x}_i \in \mathbb{R}^d$ and associated labels $y_i \in \{\pm 1\}$, $i = 1, \ldots, M$. The goal is to find the best separating hyperplane parametrized by a *normal vector* $\boldsymbol{w}$ and an *offset*

b; finding this hyperplane can be formulated as an optimization problem

$$\min_{\boldsymbol{w},b,\boldsymbol{\xi},\rho} \frac{1}{2}\|\boldsymbol{w}\|_2^2 - \nu\rho + \frac{1}{M}\sum_{i=1}^{M}\xi_i \qquad (1)$$
$$s.t.\ y_i\left(\boldsymbol{w}^T\phi(\boldsymbol{x}_i) + b\right) \geq \rho - \xi_i,$$
$$\xi_i \geq 0,\ \rho \geq 0,$$

where ξ_i, $i = 1,\ldots,M$, are slack variables that allow some misclassifications during training, and ϕ is a function lifting a sample into feature space. We decided to use this variant because it is equivalent to the commonly used C-SVM [28] and according to [27] the hyperparameter $\nu \in (0,1]$ can be bounded from above by

$$\nu \leq \nu_{\max} := \frac{2}{M}\ \min\{\#\{y_i = +1\}, \#\{y_i = -1\}\} \leq 1,\ (2)$$

where $\#\{y_i = \pm 1\}$ denotes the number of samples labeled $+1$ and -1, respectively. In the application, we used the well-known LIBSVM library for solving a SVM optimization problem of the above form, which actually aims to solve the according dual problem

$$\min_{\boldsymbol{\alpha}} \frac{1}{2}\boldsymbol{\alpha}^T\boldsymbol{Q}\boldsymbol{\alpha}$$
$$s.t.\ 0 \leq \alpha_i \leq \frac{1}{M}, \quad i = 1,\ldots,M$$
$$\mathbf{1}^T\boldsymbol{\alpha} \geq \nu,\ \boldsymbol{y}^T\boldsymbol{\alpha} = \mathbf{0},$$

where $\boldsymbol{Q}_{i,j} = y_i y_j k(\boldsymbol{x}_i, \boldsymbol{x}_j)$, $i,j = 1,\ldots,M$, is a matrix encoding the kernelization for a kernel k. In the application we use a Gaussian kernel, i.e.,

$$k(\boldsymbol{x}, \boldsymbol{y}) = \langle\phi(\boldsymbol{x}), \phi(\boldsymbol{y})\rangle = \exp\left(-\gamma\|\boldsymbol{x} - \boldsymbol{y}\|^2\right) \qquad (3)$$

with an additional kernel bandwidth parameter $\gamma > 0$. Support Vector Machines have the special advantage that after the training only few samples $\boldsymbol{x}_j$, $j = 1,\ldots,M'$, where $M' \leq M$, really contribute to the prediction. These samples are named *support vectors* as they lie on the boundary of the margin along the trained hyperplane. This condition implies that $\alpha_j > 0$, $j = 1,\ldots,M'$, for these samples. A trained SVM then can predict a label from its support vector representation by

$$\mathcal{S}^u(\boldsymbol{x}) = \sum_{i=1}^{M} y_i\alpha_i k(\boldsymbol{x}, \boldsymbol{x}_i) + b$$

and taking the sign of the result.

In its basic form, an SVM only emits a label, which by our problem formulation is either $+1$ or -1. In practice, we prefer a probabilistic prediction of how likely it is that a given voxel is part of the component to be segmented and this information shall be present in the segmentation result. This type of output is achieved by using Platt scaling [29] which fits a sigmoidal curve to the distribution of distances to the separating hyperplane obtained after training. The goal of Platt scaling is to find a parametrization of this sigmoidal curve using logistic regression such that it creates a calibrated probabilistic estimation $\mathcal{S}(\boldsymbol{x}) := P\left(y_i = +1 \mid \mathcal{S}^u(\boldsymbol{x})\right)$. In the sequel, we will refer to such estimates as *confidence values*.

3.3 Hyperparameter Tuning

The ν-SVM problem still contains two hyperparameters, i.e., parameters occuring in the problem formulation that are not optimized by the solver itself but have to be tuned manually. In our formulation, these remaining variables are the value ν in (1) that determines how tolerant the SVM is towards misclassifications and the localization parameter γ in the kernel function k in (3). In [28], it was shown that ν is "*an upper bound on the fraction of margin errors and a lower bound of the fraction of support vectors*" and that these two fractions coincide with probability 1. Therefore, ν effectively serves as a trade-off between misclassifications and sparsity of the model. Clearly, the value of ν is contained in the unit interval, and we already mentioned that it can be bounded from above by $\nu_{\max}$ as given in Equation (2). In order to find a good value for this hyperparameter, we sample the feasible region $(0, \nu_{\max}]$ equidistantly. On the other hand, $\gamma > 0$ is the kernel bandwidth parameter inversely proportional to the variance of the Gaussian kernel function. As is common practice, we create for it a parameter set on a logarithmic scale. The boundaries for both sets in the real applications were determined experimentally. Then, the overall hyperparameter grid is given as $P = P_\nu \times P_\gamma$. From this, we determine the best hyperparameter grid point $(\nu^*, \gamma^*) \in P$ using C-fold cross validation where $C = 7$ turned out to be suitable in our applications.

3.4 Why Support Vector Machines?

In principle, the classifier need not be a Support Vector Machine and one could try more fancy techniques of machine learning, so we briefly want to state why we decided to choose an SVM. First of all, its most important advantage is that only a small number of data points is necessary to make a prediction, which saves both runtime as well as memory and makes SVMs especially well-suited for our active learning approach: a robust hyperplane can be trained with few samples, i.e., with a small number of seed voxels. This keeps the amount of user interaction very moderate. Another advantage is that we could encode our geometric knowledge about local regions in our features, which are thus designed such that visually similar regions produce feature vectors that are close with respect to the Euclidean distance and thus pair well with our choice of a Gaussian kernel. The nonlinearity in the Gaussian kernel enables the construction of complex separation surfaces which still fit into the hyperplane framework in the kernel space.

Furthermore, support Vector Machines are known to provide a good out-of-sample generalization, i.e., bias contained in the training dataset can be somewhat compensated by appropriate hyperparamter tuning [30]. Finally, the low memory consumption makes SVMs attractive to be serialized and applied to other datasets. Although in practice a pretrained model will rarely be a good classifier for an unrelated and unseen dataset, a simple retraining method can be formulated by serializing all unscaled feature vectors. Upon retraining, the serialized representation is loaded from disk and combined with the newly provided samples which forms the new training data. This simple and straightforward approach gave more than satisfactory results in many of our applications.

3.5 Active Learning and Segmentation

After designing geometric features based on local voxel environments and a classifier which can be trained on them, we put everything together into a segmentation procedure based on *active learning*.

Active learning (AL) is an emerging branch in machine learning that tries to compensate a lack of annotated training data by featuring an oracle which labels samples on-the-fly. Examples for such oracles are additional machine learning techniques or in our and many other applications a human annotator. The basic concept is that some samples are labeled by the oracle, and a model is trained from them. This trained model then predicts results which render some samples as ambiguous, i.e., the model cannot make a clear prediction about this sample. The ambiguous samples are then returned to the oracle to be labeled. This process is continued until the results are stable or good enough. There exist different approaches for querying the oracle with samples that are either generated by the model *de novo* or stem from a stream or a pool of existing samples. In the literature, a variety of techniques for detecting ambiguous samples can be found, including *uncertainty sampling*, in which an uncertainty measure determines the samples which the model is most uncertain about, *query-by-committee*, where the samples are selected on which the majority of the classifiers disagree, or *estimated error reduction* which selects the sample that minimizes the generalization error of the model, cf. [6].

Applied to voxelwise segmentation, active learning would imply that our model queries a user to label small local voxel environments. As this is impractical, we instead follow a pool-based approach in which a trained model segments the entire voxel volume. Using a priori information this could be restricted to selected regions only, however the definition and handling of such information is highly application specific and out of scope of our work here. Next, ambiguous samples are detected by uncertainty sampling, computed from our confidence value predictions. In our setting of segmenting very large three-dimensional volumes, more advanced sample query strategies, e.g., estimated error reduction, are too computationally expensive. To perform uncertainty sampling, we compute an uncertainty value from a confidence value as follows.

Definition 2. For a *confidence value* $\mathcal{S}(\boldsymbol{x}) \in [0, 1]$ and $\delta \geq 0$, we define the *uncertainty value* $\mathcal{U}(\boldsymbol{x})$ as

$$\mathcal{U}(\boldsymbol{x}) = \exp\left(-\delta \tan\left(\pi \left|\mathcal{S}(\boldsymbol{x}) - \frac{1}{2}\right|\right)\right).$$

By this definition of the confidence values, we know that the model is most uncertain about samples which lie close to the separating hyperplane and thus produce a confidence value close to $1/2$. The uncertainty values define a Gaussian window around this confidence value where δ controls the width of that bell curve.

The segmentation procedure is repeated until the results are of sufficient quality, and it is summarized in Algorithm 1. The framework is a follows: We start with an input volume V of dimensions $\boldsymbol{d} \in \mathbb{N}^3$ that is assumed to consist of voxels located at the regular *grid positions* $\boldsymbol{\alpha} \leq \boldsymbol{d}$ with values $x_{\boldsymbol{\alpha}} \geq 0$. The generated output volume $\widetilde{V}$ is of same size as V and its voxel values are denoted by $\widetilde{x}_{\boldsymbol{\alpha}}$. In a

---

Algorithm 1: AL Volume Segmentation

Input : Input volume V
Input : Feature computation function F
Output: Output volume $\widetilde{V}$

$(f_i, L_i) \leftarrow$ de-serializ. // opt., default $((),())$
$U \leftarrow V$
repeat
  $(f_n, L_n) \leftarrow$ features and labels, selected using U
  $f_i \leftarrow (f_i, f_n)$
  $L_i \leftarrow (L_i, L_n)$
  Train SVM using features f_i and labels L_i
  Serialize trained model   // opt.
  forall $\boldsymbol{\alpha} \leq \boldsymbol{d}$ **do**
    $E \leftarrow K \times K \times K$ environment around $\boldsymbol{\alpha}$
    $\widetilde{x}_{\boldsymbol{\alpha}} \leftarrow \lfloor 100\,\mathcal{S}(F(E)) \rfloor$
  $U \leftarrow$ uncertainty volume from confidence values
until $\widetilde{V}$ *is satisfactory*

---

first (optional) step, serialized feature vectors and associated labels can be read from disk. Next, an oracle selects voxels of high uncertainty and labels them either positively ($+1$ = "belongs to the relevant component") or negatively (-1 = "does not belong not to the component"), where the selection is focussed on visual input from the original voxel volume. In subsequent iterations, the uncertainty volume U hints about regions where the model is unsure and from which the oracle can select further samples. Around each selected sample a small local voxel environment is extracted from which features f_n are computed. Then a Support Vector Machine is trained using all feature vectors and their labels. This step also includes training the feature vector scaler, the hyperparameter tuning as well as Platt scaling. After this training is completed, all voxels for which a full local region can be extracted are investigated in a single pass, where, again, a small voxel environment E is extracted around each of them, and features are computed from which the SVM predicts a confidence value $\mathcal{S}(F(E))$ which is scaled to percent. From this confidence, an uncertainty volume can be computed according to Definition 2, which hints to the oracle where to choose the next samples. This process is repeated until the results are satisfactory.

To illustrate the interactive procedure we consider a CT scan of a Mahle motor piston and aim to segment the steel ring located near the top. The process took four iterations, the intermediate results are depicted in Figure 2 in which brighter colors indicate higher values of the CT grayscale. In the initial iteration, we interactively selected *two* seed voxels in the steel ring regions to be marked as positive and additionally chose two seed voxels in the aluminum regions of the piston, marked as negative. After applying the segmentation, we then obtain a volume consisting of confidence values from which we compute uncertainty volumes. Both the confidence and uncertainty values in the images shown in Figure 2a indicate that the model is highly unsure about decision making.

We next use these uncertainty values as an indication where to select additional seed voxels and apply Algo-

rithm 1 again, see Figure 2b. The results improve by a magnitude as now confidences are high at the steel ring while they are low for the other piston voxels. The uncertainty is only concentrated at the border of the datasets to separate. We continue this for two further iterations during which the confidence values stabilize and the uncertainty decreases.

After four iterations, the uncertainty is mostly gone, thus signaling that we can now stop selecting voxels. A simple thresholding on the confidence values then yields the desired segmentation result.

3.6 Runtime and Memory Analysis

Since we especially focus on processing large volumetric data, we briefly analyze the asymptotic runtime and memory behavior. Reading serialized data from disk is optional and can be considered as an operation with a constant runtime. The next step selects $M \in \mathbb{N}$ seed voxels and computes feature vectors from local environments of the seed voxels, which are used for training a Support Vector Machine. The training procedure for a SVM is reported to be typically of quadratic or cubic order, depending on its hyperparameters cf. [31, p.10]. Our training step includes a grid search hyperparameter tuning where for each parameter a C-fold cross validation is executed. Therefore, the overall runtime necessary for our training step scales with $\#P\,C\,\mathrm{poly}(M/C)$. After the training is completed, we iterate over the volume in a single linear pass and perform the voxelwise classification. That step is linear in terms if the number $N \in \mathbb{N}$ of voxels. Note that the computation of the uncertainty volume may be not be executed at all if, e.g., an application decides to simply use the confidence values directly for indication where to select voxels next. If it is used, it is again linear in N. That interactive procedure is repeated until the result is satisfactory after $I \in \mathbb{N}$ iterations. Again, the optional final serialization step has a constant runtime. In summary, the overall runtime behavior of Algorithm 1 is

$$\mathcal{O}\left(I\left(\frac{\#P}{N_T}\,C\,\mathrm{poly}(M/C) + N\right)\right),$$

where typically $\deg \mathrm{poly}(M/C) \leq 3$ and N_T denotes the number of threads available on the executing system since the grid search trainings can be executed independently from another. Since C, P and N_T are fixed a priori and since we expect the number M of seed voxels to be typically far smaller (typically by orders of magnitude) and *independent* of N, the runtime is effectively linear in the number of iterations and the number of voxels, even in our pessimistic worst case estimate. This makes our procedure especially well-suited for processing very large volumetric datasets where only asymptotically linear algorithms w.r.t. to N are considered applicable.

Regarding memory consumption, we note that our segmentation procedure first needs to compute the feature vectors of dimensionality d for all M seed voxels and needs to keep these in memory at all times. The memory usage during training the model is roughly dominated by computing the kernel matrix of the dual problem formulation, which is naively of size M^2. While implementation issues might improve upon this, e.g., using a sparse matrix representation if possible, the dominating factor is still quadratic in the number of seed voxels. During the voxelwise classification only local environments centered around the currently processed voxel and the trained model are necessary, i.e., we need the M trained weight coefficients and the local environment of constant size. In total, the memory consumption is of order $\mathcal{O}\left(M^2 + Md + M\right)$. Since M is again expected to be small and independent of the number of voxels, our approach is well-suited even for segmentation of large voxel volumes which no longer fit into the main memory of a computer.

3.7 Multiresolution Segmentation

By design, our method is effectively a linear pass over the input volume which makes it applicable to volumes without size restrictions while at the same time being as efficient as possible for voxelwise segmentation. However, its execution time clearly increases linearly in the volume size which means cubically in the resolution. However, in practice the components to be found in and segmented from the volume are often relatively small compared to the overall dataset. Thus, the idea of multiresolution processing arises naturally.

While some related work considers a multiscale hierarchy to extract features and perform a classification on the full dataset, cf. [32], [33], our focus lies on segmenting only *relevant* regions. In a similar spirit, [34] segments image stacks based on a Wavelet transform using an expectation-maximization-based approach. Specifically for 3D volumes, [35] proposed a segmentation method on the coarsest level of a Gaussian pyramid and then refines the results on finer levels. In connection with interactive segmentation very few papers were published of which we mention [36] and [37]. [36] proposes an interactive shape model which uses features extracted across multiple resolutions but processes the data in its original format. Closest to our approach is the work in [37], where retinal image data is segmented progressively using simple color information.

Unfortunately, common hierarchical representations need be serialized to disk, which is exactly what we want to avoid here. Instead, we implemented a local multiresolution framework in which each voxel value currently necessary is computed ad hoc. To describe our apporoach in detail, let $V^{\ell'}$ be a volume of dimensions $\boldsymbol{d} \in \mathbb{N}^3$ at resolution level $\ell' \in \{1, \ldots, \ell_{\max}\}$, where $\ell_{\max} \in \mathbb{N}$ denotes the number of resolution levels available for this volume. Assume that it consist of voxels located at a grid $\boldsymbol{\beta} \leq \boldsymbol{d}$ having values $x_{\boldsymbol{\beta}}$. We now wish to interpret such a volume as a volume at a coarser resolution level $\ell \in \{1, \ldots, \ell'\}$. To that end, a voxel at position $\boldsymbol{\alpha}$ in the coarse grid is said to *cover* a set of voxels in the fine grid which are combined for its computation. Formally, we define the set of its covered voxel positions by

$$\mathfrak{S}_{\ell'}^{\ell}(\boldsymbol{\alpha}) = \left\{\boldsymbol{\beta} \leq \boldsymbol{d} \mid \boldsymbol{\beta} = 2^{\ell'-\ell}\boldsymbol{\alpha} + \boldsymbol{\kappa},\ |\boldsymbol{\kappa}| \leq 2^{\ell'-\ell} - 1\right\}$$

which encompasses $8^{\ell'-\ell}$ high-resolution voxels in total. Like in Haar wavelet computations, the grayscale value of any voxel at position $\boldsymbol{\alpha} \leq 2^{\ell'-\ell}\boldsymbol{d}$ on a coarser resolution level is then computed as the arithmetic mean of the voxel values covered by it:

$$x_{\boldsymbol{\alpha}} = 8^{\ell-\ell'} \sum_{\boldsymbol{\beta} \in \mathfrak{S}_{\ell'}^{\ell}(\boldsymbol{\alpha})} x_{\boldsymbol{\beta}}.$$

(a) Iteration #1

(b) Iteration #2
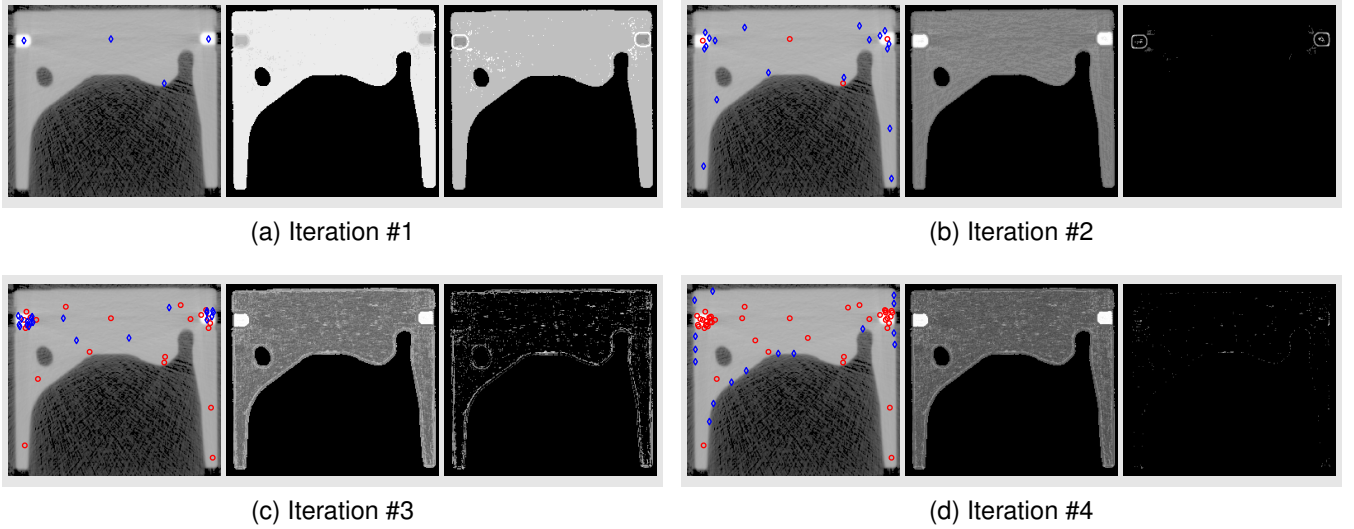
(c) Iteration #3

(d) Iteration #4

Fig. 2. Applying Algorithm 1 to a motor piston dataset, showing four iterations. In all images contrast was enhanced for better visibility, brighter shades indicate higher values. (a) shows the setting of the first iteration in which first the voxel selection is shown, new ones by blue diamonds and already selected ones by red circles. Its middle image depicts the predicted confidence values and to its right the computed uncertainty values are visualized. This is best viewed in color. (b), (c) and (d) show the next three iterations, respectively.

Typically, we perform this on-the-fly computation at coarse resolutions ℓ directly from the finest resolution level, i.e., the actual grayscale data, thus in our application we work with $\ell' = \ell_{\max}$.

Based on these *multiresolution volumes*, we can now formulate an enhanced segmentation procedure that combines the multiresolution interpretation as well as our active learning procedure. The result is listed in Algorithm 2. Also this procedure requests the labeling of additional seed voxels from which features are extracted. That feature extraction now happens on all resolution levels *simultaneously* and one specific SVM is trained for each scale. Additionally, confidence thresholds are computed which determine the minimal value to consider a voxel as a candidate. That is, during the iterations over all but the finest resolution level, the SVM related to the current resolution predicts a confidence value for any voxel in the considered regions at that resolution. If the confidence is higher than the threshold, that voxel does likely belong to the component we aim for. In our application, we search for an optimal threshold which minimizes the misclassifications, i.e.,

$$\rho_\ell = \operatorname*{argmin}_{\rho \in [0,1]} \sum_{\epsilon \in \{\pm 1\}} \frac{1}{\#\mathcal{T}_\epsilon^\ell} \sum_{\boldsymbol{x} \in \mathcal{T}_\epsilon^\ell} H\left(\epsilon\left(\rho - \mathcal{S}^\ell(\boldsymbol{x})\right)\right)$$

where $\mathcal{T}_\epsilon^\ell$, $\epsilon \in \{\pm 1\}$, denotes the positive and negative training samples at resolution ℓ, respectively, and H is the Heaviside step function. A procedure FindCandidates uses this approach by considering all voxels of V^ℓ contained in the previous set of candidates $C_{\ell-1}$ on resolution level $\ell - 1$. For each of them, the trained model m_ℓ predicts a confidence value and the currently processed voxel is remembered as a candidate if and only if that prediction lies above the confidence threshold ρ_ℓ. The set of candidate voxels is simplified periodically by organizing them into rectangular regions of interest by connectedness and scaling them to fit the volume dimensions at the next resolution level. After processing a resolution level, the candidates

---

Algorithm 2: Multiresolution segmentation

Input : Input volume V of dimensions $\boldsymbol{d}$
Input : Feature computation function F
Output: Output volume $\widetilde{V}$

$(f_i, L_i) \leftarrow$ de-serializ. // opt., default $((),())$
$U \leftarrow V$
repeat
$\quad (f_n, L_n) \leftarrow$ features and labels, selected using U
$\quad f_i \leftarrow (f_i, f_n)$
$\quad L_i \leftarrow (L_i, L_n)$
$\quad$ Train SVMs $m_\ell, \ell = 1, \ldots, \ell_{\max}$
$\quad$ Serialize trained models $\qquad\qquad$ // opt.
$\quad (\rho_\ell)_{\ell=1}^{\ell_{\max}} \leftarrow$ confidence thresholds

$\quad$ // Region localization
$\quad C_0 \leftarrow \{(\boldsymbol{0}, \boldsymbol{d})\}$
$\quad$ **for** $\ell \leftarrow 1 \rightarrow \ell_{\max} - 1$ **do**
$\quad\quad\lfloor\ C_\ell \leftarrow$ FindCandidates$(V^\ell, C_{\ell-1}, m_\ell, \rho_\ell)$

$\quad$ // Final voxelwise segmentation
$\quad$ **forall** $C \in C_{\ell_{\max}-1}$ **do**
$\quad\quad V_C \leftarrow$ voxel positions in C
$\quad\quad$ **forall** $\boldsymbol{\alpha} \in V_C$ **do**
$\quad\quad\quad E \leftarrow K \times K \times K$ environment around $\boldsymbol{\alpha}$
$\quad\quad\quad \widetilde{x}_{\boldsymbol{\alpha}} \leftarrow$ SVM prediction $m_{\ell_{\max}}(F(E))$

$\quad U \leftarrow$ uncertainty volume from confidence values
until $\widetilde{V}$ *is satisfactory*

---

obtained on that level serve as the new search locations on the next scale, and we continue until the finest resolution level on which our usual voxelwise classification takes place inside the final candidate regions. The goal is, of course, that the candidate regions encompass a relatively small subset of the regions at higher resolutions, thus reducing the number

of voxels to be considered significantly. Having processed the volume this way over all resolution levels, we again may compute an uncertainty volume and repeat the method until the result is satisfactory.

The purely local processing that is present also in the multiscale case, renders Algorithm 2 applicable to volumes without size restrictions too. Roughly, the runtime complexity of the modified algorithm depends linearly on the number of seed voxels, the runtime for the training procedure and the number of voxels inside the candidate regions found. The multiresolution procedure is intended to be used when we aim to segment relatively small parts from really big voxel scans. Naturally, if the object to be segmented fills the entire scan, a multiresolution voxelwise segmentation is not beneficial and the runtime deteriorates to be polynomial in the number of voxels. The memory consumption simply duplicates the ones derived for the single SVM case by $\ell_{\max}$ and thus still scales linearly with the number of seed voxels.

In an experiment, we segmented the springs from a computed tomography scan of a crashed car which consists of 3,171,818,496 voxels in total. The remaining regions of interest at the finest resolution level encompassed 6,281,221 voxels which amounts to roughly 0.2 percent of the overall voxel count, which demonstrates the dramatic reduction of voxels to process if the dataset is well suited for multiresolution processing.

4 RESULTS

We now illustrate the potential and the performance of our approach by means of some concrete examples. We provide a quantitative evaluation on scans where ground truth data is available, but also demonstrate the flexibility of our method on complex scans from a variety of different domains. All datasets considered were created by the Fraunhofer Development Center for X-ray Technology (EZRT) in Fürth. If necessary, additional copyright information is provided.

4.1 Quantitative Evaluation

To provide quantitative results, we apply our method in a deterministic way to seven selected datasets where ground truth data was available. These datasets are depicted in Figure 3 and Figure 5a, respectively. For each of them, we selected a fixed set of seed voxels and the parametrization shown in Table 1, including the features we used and the size K_1 of the local environments. For each dataset, we also employed a postprocessing step in form of a speckle removal, where the values of any voxels having less than η nonzero neighbor voxels in an environment of size $K_2 \times K_2 \times K_2$ are set to zero, followed by a simple connected components analysis to select the components we are interested in. These straightforward image processing operations were needed to clean up the segmentation result by removing isolated voxels that were an obvious misclassification. The results are summarized in Table 2 where we compared our segmentation results with the ground truth according to the well-known performance metrics Intersection over Union (IoU), precision, recall, and the F_1 score. These experiments clearly show that our very general

segmentation method is able to achieve good results on scans which stem from the industrial domain.

TABLE 1
Experiment setup for quantitative evaluation.

Scan	K_1	Features used	Speckle removal
Ford Fiesta	7	Grayscale + Inertia	$K_2 = 5, \eta = 15$
Piston	5	Grayscale + Inertia	$K_2 = 5, \eta = 18$
Big Piston	5	Grayscale	$K_2 = 5, \eta = 18$
Tasterwald	7	Grayscale + LBP	-
Ring	7	Grayscale + Dist. Hist.	-
Rumpf	7	Grayscale + Plane fit	-
TPA	3	Grayscale + Inertia	$K_2 = 3, \eta = 18$

TABLE 2
Quantitative evaluation results.

Scan	IoU	Precision	Recall	F_1
Ford Fiesta	0.757	0.970	0.775	0.862
Piston	0.980	0.980	1.000	0.990
Big Piston	0.985	0.980	0.997	0.992
Tasterwald	0.883	0.999	0.884	0.934
Ring	0.950	0.965	0.984	0.974
Rumpf	0.949	0.963	0.985	0.974
TPA	0.989	0.992	0.997	0.994

Influence of multiple resolution levels

Next, we analyze the influence of multiple resolution levels on quantitative segmentation results. For this purpose, we apply the same kind of evaluation over multiple resolution levels, i.e., we use the same seed voxels on all available scales, train and apply the model and again use the postprocessing specified in Table 1. The results are depicted in Figure 4. Depending on the dataset, the IoU stays approximately constant over multiple scales which shows the robustness of the approach for well-suited datasets. On the other hand, this measure deteriorates a little bit when we aim to segment objects that have a curved geometry. This observation is easily explained as especially curvature gets lost when the resolution gets coarser, thus the according regions are not considered as candidates on a coarse level and hence are not segmented on finer ones. We observed that behavior on datasets including the "Ford Fiesta" and the "Tasterwald" scan. There, our goal was to segment the springs and the small orbs, respectively. In both cases, the desired objects have considerable curvature which degrades on a coarser scale. Recall that the IoU evaluation metric is sensitive to individual misclassified voxels, which explains the smaller values when small voxel regions are not segmented using multiple resolutions. The same trend is reflected by the F_1 score evaluation although the obtained values are still high. Note that for all four different settings the same postprocessing was applied per volume. In practice, however, the postprocessing should be interactively adapted to the individual outcomes for best possible results. This, however, would reduce the comparability of the result volumes. We further measured the execution time speedups
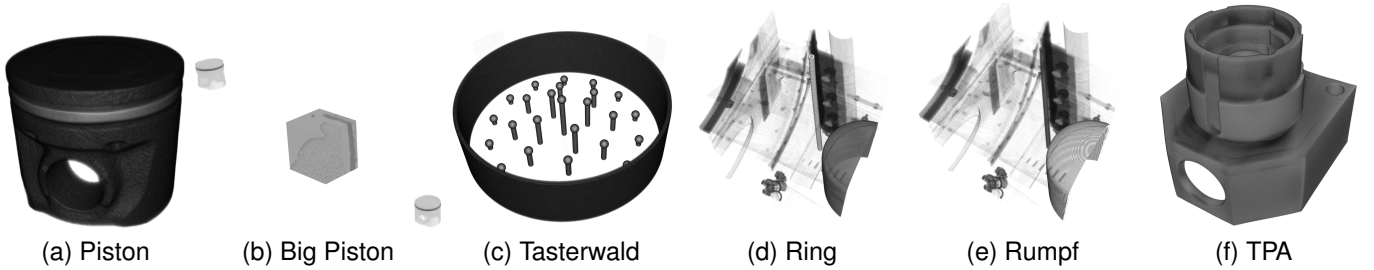
Fig. 3. Datasets for which ground truth data is available. (a) shows a Mahle motor piston, (b) incroporates this piston in with a "Leberkassemmel" data. (c) shows a calibration dataset, while (d) and (e) show individual parts of a small airplane (courtesy of *Deutsches Museum*) where the components under investigation are highlighted in white, and (f) again is a calibration dataset.

obtained when using multiple resolution levels, where we distinguished between the overall speedup including the training process, cf. Figure 4d, and the speedup on the evaluation part only, cf. Figure 4c. Since in the multiresolution case we need to train multiple models, we obtain an increase in the runtime while, at the same time, the real benefit of multiscale algorithms is obtained in the evaluation part. If datasets are well-suited for multiresolution processing as exemplary explained for the Ford Fiesta earlier, Algorithm 2 really achieves considerable speedups of up to $20\times$ over the single resolution execution. On several scans, e.g., "TPA", where nearly the entire volume consists only of the object that shall be segmented the runtime drops to about the same as in the single resolution case. But in such cases the execution might actually get slower due to the same region but more voxels need to be processed on each scale. In conclusion, the localized multiresolution processing enables and accelerates the segmentation of volumes without size restrictions and at the cost of only minor performance decreases, depending on the dataset.

4.2 Qualitative Evaluation

In order to demonstrate the flexibility of our method, we now apply it to several datasets which are large and also unique, i.e., scans with no similar scans available. Such volumes cannot easily be processed by methods like neural networks. Renderings of the datasets and the segmentation results are depicted in Figure 5, the parameter setting we used is summarized in Table 3. Again, we applied problem-specific postprocessing in form of speckle removal and connected components labeling.

TABLE 3
Qualitative evaluation setup.

Scan	Features	K_1	#Seeds (pos / neg)
Ford Fiesta	Grayscale + Inertia	3	65 / 81
Honda Accord	Grayscale + Inertia + HOG	5	110 / 142
Wheat plant	Grayscale + Inertia	7	79 / 39
Mummy	Grayscale + Inertia + Line fit	7	101 / 128

The first example is a CT scan of a crashed Ford Fiesta with the task to extract the four springs, where the front pair was actually damaged and deformed during the crash. We interactively selected some (65) seed voxels in the spring marked red in the rendering and labeled them as positive, i.e., told the system that we want to extract this component. Moreover, we marked some (81) voxels outside that spring as negative. Next, we applied Algorithm 1 with postprocessing in form of speckle removal and a connected components analysis, see previous section. The result shows the four extracted springs which were segmented using only the information from the marked one, encoded in 146 voxels in total. In another crash car, a Honda Accord, the goal was to segment a component of the frame that had been damaged during the crash. The challenge in this case is that this component has a very complex *global* geometry, locally extracted regions, however, can be successfully identified with each other and distinguished from regions that were extracted from unrelated parts of the volume. The result is overlaid in white and shows how even that complex object can be successfully segmented interactively.

Switching to an application in biology/agricultural technology, we applied our method to a scan of a wheat plant which is planted in a pot filled with earth. This scan is difficult to segment due to low contrast, many connecting components (earth, roots, small rocks) and the complex geometry on the roots. Nevertheless, the interactively obtained segmentation result was satisfactory and even able to detect many very thin roots efficiently.

Finally, in the context of cultural heritage, we consider a scan of a Peruvian mummy, data courtesy of the Lindenmuseum in Stuttgart, which is arguably the highest resolution scan ever made of a mummy, having a voxel edge length of 95 micrometers and being roughly 987 Gigabytes in size. Our focus here lied in segmenting the ropes from the scan (downsampled by a factor of 4 in each direction) which hold the bundle together. Again, we marked rope voxels and labeled them as positive while marking other voxels as negative. Since we have a priori knowledge about the structure we aim to segment, we made use of it by realizing that it is beneficial to explicitly consider the line fit feature designed to detect linear structures, c.f. Table 3. The results are clearly visible ropes and their connections, which we overlaid over the original data.

5 CONCLUSION

In industrial computed tomography there is a special interest in the task of segmentation, i.e., partitioning a large three-dimensional voxel dataset into several disjoint components with the goal of extracting information about the
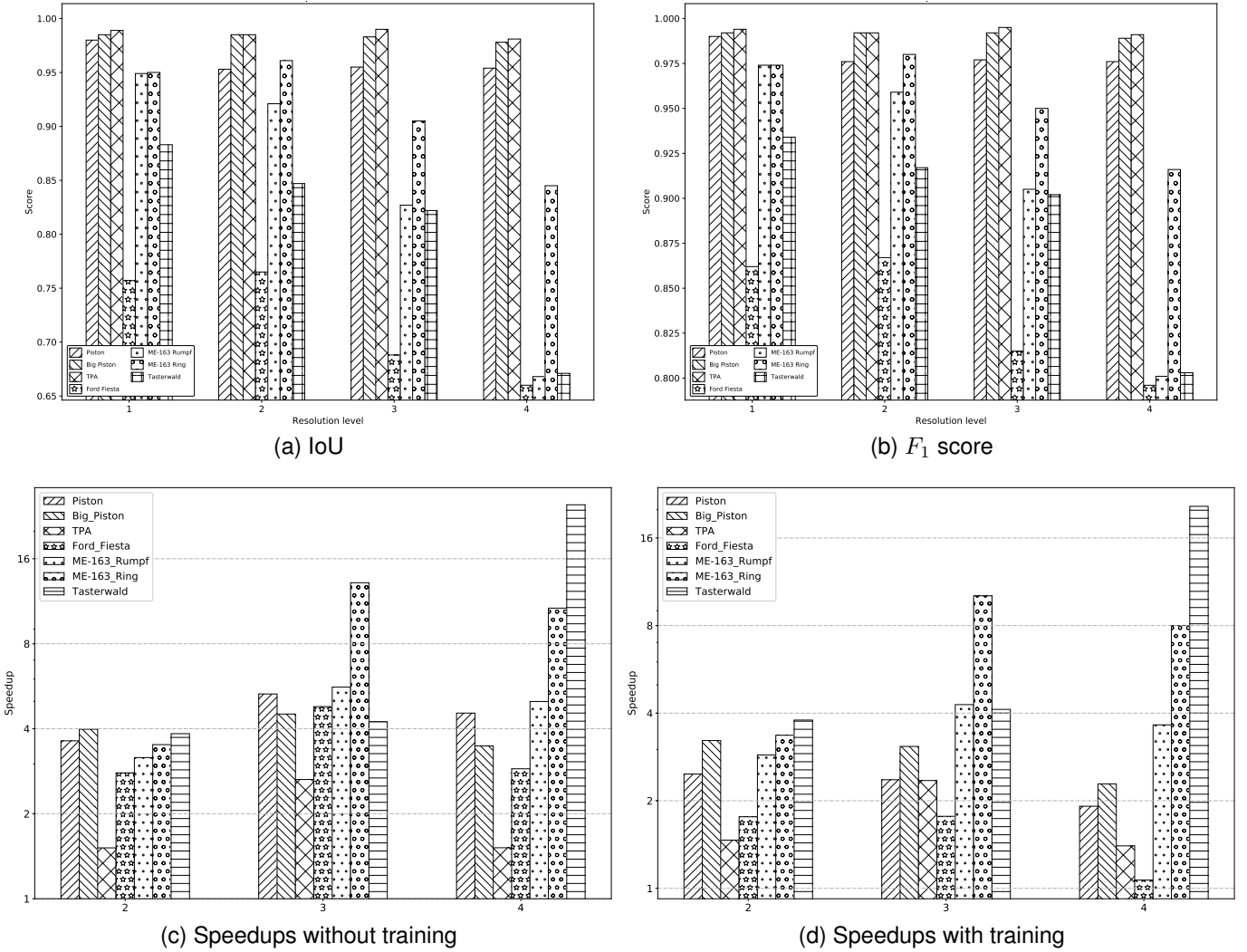
Fig. 4. Quantitative evaluation over multiple scales. (a) shows the evaluation with respect to IoU while (b) evaluates w.r.t. the F_1 score. Contrary, (c) and (d) show the speedups for the same datasets when using up to four resolution levels.

object under consideration. In this task, one faces the challenge that most modern methods require a lot of annotated training data samples which are rarely available, especially in unique scans.

We introduced a novel interactive segmentation procedure which combines active learning, geometric features and local processing. Besides giving a user a possibility at all to define *what* should be selected from the volume, the active learning part gives a flexible way of incorporating domain knowledge ad hoc into the algorithm and thus allows us to use the very same algorithm for a big variety of tasks. The very general approach of comparing local regions to geometric primitives mimics the human perception of objects and enables the application of the proposed scheme on almost any type of scan without the need to design a separate segmentation method for each component to be extracted, as is common practice, e.g., in the majority of clinical applications. Finally, the purely local processing not only simplifies computations but also renders our algorithm applicable to perform three-dimensional image processing on volumes which may be larger than main memory. This marks our procedure as one of the very first methods which

were explicitly designed to be used in the context of large tomography scans while still maintaining flexibility, since we can use it to segment many different components. On top of that we enhanced the method by a multiresolution processing algorithm which incorporates both local processing and our geometric active learning approach and enables a faster interactive processing of volumes without size restrictions. In addition, the algorithm works on *voxel datasets*, so we are not limited to computed tomography but our algorithm can be applied to any three-dimensional voxel data, also from different domains, like MRI data.

ACKNOWLEDGMENTS

(a) Original (b) Segmented (c) Original (d) Segmented

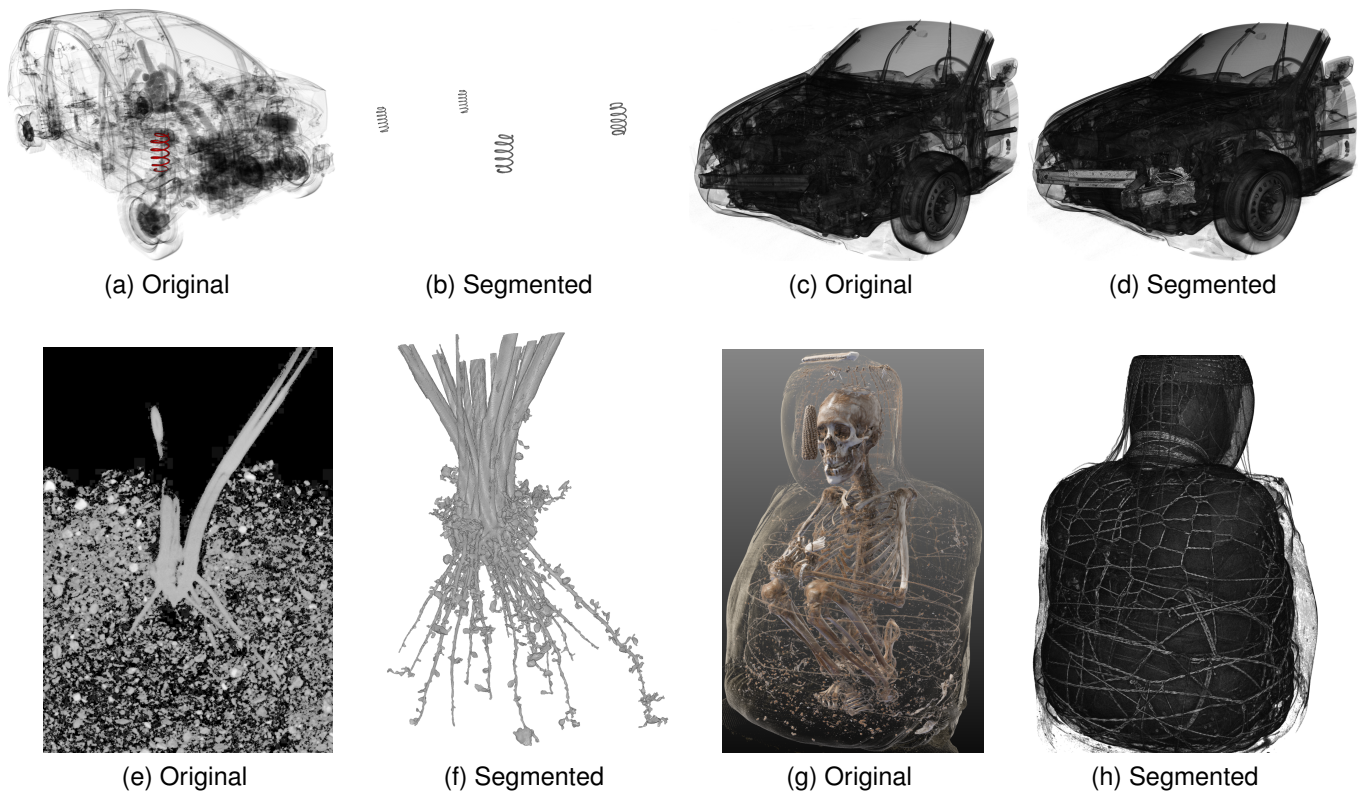(e) Original (f) Segmented (g) Original (h) Segmented

Fig. 5. Qualitative segmentation results, each showing first a rendering of the original dataset and the segmentation result. The rendering in (g) was provided by Fraunhofer MEVIS. Contrast was enhanced where necessary. In case of the mummy dataset and the second crash car, the segmented components were overlaid over the original voxel dataset. The other results are not overlaid for better visibility.

REFERENCES

[1] Ö. Çiçek, A. Abdulkadir, S. S. Lienkamp, T. Brox, and O. Ronneberger, "3D U-Net: Learning Dense Volumetric Segmentation from Sparse Annotation," in *Medical Image Computing and Computer-Assisted Intervention – MICCAI 2016*, S. Ourselin, L. Joskowicz, M. R. Sabuncu, G. Unal, and W. Wells, Eds., 2016, pp. 424–432.

[2] L. Yang, Y. Zhang, J. Chen, S. Zhang, and D. Z. Chen, "Suggestive Annotation: A Deep Active Learning Framework for Biomedical Image Segmentation," *CoRR*, vol. abs/1706.04737, 2017.

[3] Y. Siddiqui, J. Valentin, and M. Nießner, "ViewAL: Active Learning with Viewpoint Entropy for Semantic Segmentation," *CoRR*, vol. abs/1911.11789, 2019.

[4] D. Mahapatra, B. Bozorgtabar, J. Thiran, and M. Reyes, "Efficient Active Learning for Image Classification and Segmentation using a Sample Selection and Conditional Generative Adversarial Network," *CoRR*, vol. abs/1806.05473, 2018.

[5] S. Tong and D. Koller, "Support Vector Machine Active Learning with Applications to Text Classification," *J. Mach. Learn. Res.*, vol. 2, pp. 45—-66, 2002.

[6] B. Settles, "Active learning literature survey," University of Wisconsin–Madison, Computer Sciences Technical Report 1648, 2009.

[7] J. Kremer, K. Steenstrup Pedersen, and C. Igel, "Active Learning with Support Vector Machines," *WIREs Data Min. Knowl. Discov.*, vol. 4, no. 4, pp. 313–326, 2014.

[8] L. Wang, K. L. Chan, and Z. Zhang, "Bootstrapping SVM active learning by incorporating unlabelled images for image retrieval," in *IEEE Computer Society Conference on Computer Vision and Pattern Recognition*, 2003, pp. 629–634.

[9] G. Matasci, D. Tuia, and M. Kanevski, "Svm-based boosting of active learning strategies for efficient domain adaptation," *IEEE Journal of Selected Topics in Applied Earth Observations and Remote Sensing*, vol. 5, no. 5, pp. 1335–1343, 2012.

[10] H. Veeraraghavan and J. V. Miller, "Active Learning Guided Interactions for Consistent Image Segmentation with Reduced User Interactions," in *IEEE International Symposium on Biomedical Imaging: From Nano to Macro*, 2011, pp. 1645–1648.

[11] B. Mathieu, A. Crouzil, and J. Puel, "Interactive multiclass segmentation using superpixel classification," *CoRR*, vol. abs/1510.03199, 2015.

[12] X. Zhang, J. Tian, D. Xiang, X. Li, and K. Deng, "Interactive liver tumor segmentation from ct scans using support vector classification with watershed," in *Annual International Conference of the IEEE Engineering in Medicine and Biology Society*, 2011, pp. 6005–6008.

[13] K. Konyushkova, R. Sznitman, and P. Fua, "Geometry in Active Learning for Binary and Multi-class Image Segmentation," *Comput. Vis. Image Underst.*, vol. 182, pp. 1–16, 2019.

[14] F. Song, Z. Guo, and D. Mei, "Feature Selection Using Principal Component Analysis," in *International Conference on System Science, Engineering Design and Manufacturing Informatization (IC-SEM)*, vol. 1, 2010, pp. 27–30.

[15] P. Pebay and P. Pierre, "Formulas for Robust, One-Pass Parallel Computation of Covariances and Arbitrary-Order Statistical Moments," U.S. Department of Energy, Office of Scientific and Technical Information, Tech. Rep., 2008.

[16] G. Zhao and M. Pietikäinen, "Dynamic Texture Recognition Using Local Binary Patterns with an Application to Facial Expressions," *IEEE Trans. Pattern Anal. Mach. Intell.*, vol. 29, pp. 915–28, 2007.

[17] O. Lahdenoja, J. Poikonen, and M. Laiho, "Towards Understanding the Formation of Uniform Local Binary Patterns," *ISRN Mach. Vis.*, vol. 2013, 2013.

[18] ——, "Towards Understanding the Formation of Uniform Local Binary Patterns," *ISRN Mach. Vis.*, vol. 2013, 2013.

[19] H. Yoshida and J. Näppi, "Three-Dimensional Computer-Aided Diagnosis Scheme for Detection of Colonic Polyps," *IEEE Trans. Med. Imaging*, vol. 20, no. 12, pp. 1261–1274, 2001.

[20] S. J. Ahn, *Least Squares Orthogonal Distance Fitting of Curves and Surfaces in Space*, ser. Lect. Notes Comput. Sci. Springer, 2004, vol. 3151.

[21] B. Jähne, *Spatial-Temporal Image Processing, Theory and Scientific Applications*. Springer-Verlag Berlin Heidelberg, 1993.

[22] A. Bhalerao and R. Wilson, "A Fourier Approach to 3D Local Feature Estimation from Volume Data," *Proceedings of BMVC 2001*, 04 2002.

[23] E. Kreyszig, *Advanced Engineering Mathematics*, 10th ed. Wiley, 2011.

[24] P. Billingsley, *Probability and Measure*, 3rd ed., ser. Series in Probability and Mathematical Statistics. Wiley, 1995.

[25] Panaretos, Victor and Zemel, Yoav, *An Invitation to Statistics in Wasserstein Space*. Springer, 2020.

[26] C. Cortes and V. Vapnik, "Support-vector networks," *Mach. Learn.*, vol. 20, pp. 273–297, 1995.

[27] C.-C. Chang and C.-J. Lin, "LIBSVM: A library for support vector machines," *ACM Trans. Intell. Syst. Technol.*, vol. 2, pp. 1–27, 2011.

[28] ——, "Training ν-Support Vector Classifiers: Theory and Algorithms," *Neural Comput.*, vol. 13, no. 9, pp. 2119—-2147, 2001.

[29] J. C. Platt, "Probabilistic Outputs for Support Vector Machines and Comparisons to Regularized Likelihood Methods," in *Advances in Large-Margin Classifiers*. MIT Press, 1999, pp. 61–74.

[30] L. Auria and R. A. Moro, "Support Vector Machines (SVM) as a Technique for Solvency Analysis," DIW Berlin, German Institute for Economic Research, Discussion Papers of DIW Berlin 811, 2008.

[31] L. Bottou, O. Chapelle, D. DeCoste, and J. Weston, *Support Vector Machine Solvers*. MIT Press, 2007, pp. 1–27.

[32] Y. Wang and M. Yin, "Multiresolution and multiscale geometric analysis based breast cancer diagnosis using weighted svm," in *Proceedings of the 2015 International Conference on Mechanical Science and Engineering*. Atlantis Press, 03 2016, pp. 373–378.

[33] H. Akbari and B. Fei, "3d ultrasound image segmentation using wavelet support vector machines," *Med Phys*, vol. 39, no. 6, pp. 2972–2984, 6 2012.

[34] M. A.-M. M. Salem, "Multiresolution image segmentation," Ph.D. dissertation, Humboldt-Universität zu Berlin, Mathematisch-Naturwissenschaftliche Fakultät II, 2008.

[35] C. C. Reyes Aldasoro and A. Bhalerao, "Volumetric texture segmentation by discriminant feature selection and multiresolution classification," *IEEE Transactions on Medical Imaging*, vol. 26, no. 1, pp. 1–14, 2007.

[36] A. R. Fuller, R. Zawadzki, S. Choi, D. F. Wiley, J. S. Werner, and B. Hamann, "Segmentation of three-dimensional retinal image data," *IEEE Transactions on Visualization and Computer Graphics*, vol. 13, 2007.

[37] M. de Bruijne, B. van Ginneken, M. A. Viergever, and W. J. Niessen, "Interactive segmentation of abdominal aortic aneurysms in cta images," *Med. Image Anal.*, vol. 8, no. 2, pp. 127–138, 2004.

Thomas Lang received his PhD degree in computer science from the University of Passau in 2021 for research in image segmentation. Currently, he is working as a Post-Doc in the Fraunhofer IIS Research Group on "Knowledge-Based Image Processing". His research interests include image processing of huge data, image segmentation and artificial intelligence.

Tomas Sauer received his PhD degree in mathematics from the University of Erlangen-Nürnberg in 1993 for research in Approximation Theory. From 2000 to 2012, he was professor for Numerical Mathematics/Scientific Computating at the University of Gießen. Since 2012, he holds the chair for Mathematical Image Processing at the University of Passau and is also director of the Applied Research Institute FORWISS and of the Fraunhofer IIS/EZRT Research Group on "Knowledge-Based Image Processing". His current research interests include, among others, signal and image processing for huge data, tomography, machine learning, sparse reconstructions, and continued fractions.